Analytical and numerical modeling of sandbanks dynamics

Déborah Idier[1] and Dominique Astruc
Institut de Mécanique des Fluides de Toulouse, Toulouse, France

Received 5 November 2001; revised 19 July 2002; accepted 1 November 2002; published 1 March 2003.

[1] Linear and nonlinear behavior of large-scale underwater bedform patterns like sandbanks are studied using linear stability analysis and numerical modeling. The model is based on depth-integrated hydrodynamics equations with a quadratic bottom friction law and a bed load sediment transport model including a bottom slope effect. First, the linear stability analysis of a flat erodible bottom subject to a steady current is performed. The direction of the most amplified bedform is controlled by the current, whereas its wavelength is selected by the gravity driven sediment flow. The instability proved to be due to the velocity component parallel to the mean flow, whereas the transverse velocity and the bottom slope effect are damping processes. The growth rate is then related to the spatial phase-lag between flow velocity and bathymetry. In order to validate the numerical model in this linear regime, the growth rate and the phase celerity of an infinitesimal bottom perturbation are computed as a function of its wavevector. A good agreement with linear stability results is found. Second, using the property that the growth rates for block-function and steady current are the same, the nonlinear behavior of the instability is investigated for a simple tidal current. The saturation height of the theoretically most amplified mode is estimated using the numerical model. The analysis of the sediment fluxes gradients shows that the saturation is mostly due to the hydrodynamic processes, although the saturation height slightly depends on the value of the bottom slope effect coefficient. Third, a Landau equation, whose coefficients are computed from the previous results, is used to predict the temporal evolution of the bedform amplitude from the initial infinitesimal perturbation to the saturation. A comparison with the characteristics of continental shelf sandbanks shows that the model gives a reasonable estimation of the temporal dynamics of these large-scale bedforms. However, the saturation height seems to be slightly overestimated. The limitations of the method are also discussed. *INDEX TERMS:* 3022 Marine Geology and Geophysics: Marine sediments—processes and transport; 3220 Mathematical Geophysics: Nonlinear dynamics; 4219 Oceanography: General: Continental shelf processes; 4255 Oceanography: General: Numerical modeling; 4512 Oceanography: Physical: Currents; *KEYWORDS:* sandbanks, morphodynamics, numerical modeling, stability analysis, saturation, North Sea

Citation: Idier, D., and D. Astruc, Analytical and numerical modeling of sandbanks dynamics, *J. Geophys. Res.*, *108*(C3), 3060, doi:10.1029/2001JC001205, 2003.

1. Introduction

[2] Subtidal bedforms, like sandbanks, sand ridges and sand waves, are large scale sedimentary structures with wavelengths larger than the water depth which are commonly observed on continental shelves [*Dyer and Huntley*, 1999]. All these patterns are of significant practical importance for navigation safety as they may invade navigation channels [*Le Bot et al.*, 2000] and for seabed pipeline stability [*Moshagen et al.*, 1997]. The knowledge of the morphology and the dynamics of these large-scale structures is therefore an important issue. If they may exist as isolated structures, they more likely occur as rhythmic, almost periodic, patterns.

[3] Typical sandbanks are encountered in the southern bight of the North Sea and near the Norfolk coast. Their wavelengths are of the order of several kilometers and their typical height is tens of meters. In the North Sea, their maximum height is about 40 m above the bottom [*Eisma et al.*, 1979], the maximum length is 65 km and the width is about 2 km. Their cross-sections are usually slightly asymmetrical and may be covered by megaripples or sand waves systems. Their crests are rotated from 10° to 30° with respect to the main tidal current direction.

[4] The origin of these rhythmic structures is now related to free instabilities resulting from the interaction of the flow and the sandy erodible sea bottom (see [*Blondeaux*, 2001] for a review). *Huthnance* [1982] was the first to study sandbanks generation in coastal seas using linear stability analysis techniques. He analyzed the stability of a flat

[1]Now at Faculty of Engineering, Water Engineering and Management, University of Twente, Enschede, Netherlands.

0148-0227/03/2001JC001205$09.00

bottom subject to a rectilinear two-dimensional shallow-water tidal flow. Assuming bed load sediment transport only, he succeeded in finding unstable modes with wavelengths and crests orientations close to those of natural sandbanks. The same kind of structures may also appear as unstable modes for a steady flow [*Fluit and Hulscher*, 2002]. The work of *Huthnance* [1982] has been extended by *Hulscher* [1996], who introduced a three-dimensional description of an elliptic tidal flow and showed that unstable modes included sand waves in addition to sandbanks. This model has been tested against observations of North Sea sand waves and sandbanks [*Hulscher and van den Brink*, 2001] and proved its reliability. Another three-dimensional model for tidal flows has been proposed by *Blondeaux et al.* [2000], who also take into account the presence of wind waves. Both suspended load and bed load sediment transport are included. This model also features unstable tidal sandbanks and sand waves.

[5] Although the linear stability analysis gives valuable results on the instability mechanisms, unstable modes and amplification rates, this technique is limited to infinitesimal perturbations. The dynamics of large-amplitude continental shelf bedforms has to be studied by another approach.

[6] *Calvete et al.* [1999] derived a low-dimensional dynamical system to study the nonlinear dynamics of several linearly unstable sand ridges generated by a steady current. They showed that depending on the model parameters, the finite amplitude dynamics may be dominated by the linearly most unstable mode or by another mode. Using an analytical weakly nonlinear technique, *Komarova and Newell* [2000] modeled the nonlinear behavior of the sand wave instability and showed that nonlinear interactions among unstable sand wave modes may generate sandbanks. Using a Landau equation and a genetic algorithm to estimate the equation parameters and the initial state of the model from field measurements, *Knaapen et al.* [2001] predict the growth of dredged sand waves.

[7] Besides these techniques, one can solve the conservation equations for momentum, water and sediment masses using a numerical morphodynamical model. Although these models are often used for engineering purposes [*De Vriend et al.*, 1993a], their use for large-scale bottom patterns analysis is not well developed. This kind of model offers several advantages since all the nonlinear processes which occur in finite amplitude bedforms dynamics are included. They can be used in principle to forecast the dynamics of bed patterns from generation to saturation. These models can also handle complex situations for which no analytical technique is suitable. However, the large computational time needed by these numerical models imposes some limitations in the study of long-term behavior of bedforms dynamics.

[8] In this paper, we introduce a two-dimensional morphodynamical model based on a bottom evolution equation using a generic formula for bed load sediment flux, coupled with a depth-integrated shallow-water formulation, including a quadratic friction law, for the fluid flow. This kind of 2DH model proved its relevance for the sandbanks study in the linear regime [*Huthnance*, 1982].

[9] The first goal of this work is to show that the numerical model is accurate enough to properly simulate the dynamics of the bottom free instability waves and at the same time to analyze the physical mechanisms of the instability. This is achieved for a steady current over a flat bottom. For these two purposes, based on the model equations, a linear stability analysis is performed first. This simple base state features unstable modes with geometrical properties close to those of continental shelf sandbanks [*Fluit and Hulscher*, 2002].

[10] The second goal of this work is to gain some insights into the finite-amplitude dynamics of large bottom perturbations, and in particular into the saturation process, with the numerical model. Using the property that the growth rates for a steady current and for a block-function current are the same [*Fluit and Hulscher*, 2002], the numerical computations are performed for a steady flow and the results analyzed from a tidal-flow perspective. The numerical model is used to estimate the saturation amplitude of the linearly most unstable mode. Some insights into the physical mechanisms of saturation are gained. Then, using the estimated growth rate and saturation height of the linearly most amplified mode, a Landau equation is used to compute the time evolution of its amplitude from generation to saturation.

[11] The third goal is to compare the model results to real sandbanks data and to perform an assessment of the model assumptions in order to estimate the model limitations.

[12] The present paper is organized as follows. Section 2 gives an overview of the morphodynamical model. Section 3 deals with the generation of large-scale bedforms including the linear stability analysis, the analysis of the instability mechanism and the results of the numerical model. Section 4 is devoted to finite amplitude dynamics of the linearly most-amplified mode. The applicability of these results to sandbanks dynamics is discussed in section 5, and conclusions are drawn in the last section.

2. Morphodynamical Numerical Model

[13] The two-dimensional morphological model relies on a bed evolution model coupled with a hydrodynamic model.

2.1. Bed Evolution Model

[14] The bed evolution model is based on the sediment mass conservation equation,

$$\frac{\partial h}{\partial t} = -\vec{\nabla}.\vec{S}_b, \tag{1}$$

where h is the bed position with respect to the undisturbed bed level ($z = -H$) (see Figure 1) and $\vec{S}_b$ is the bed load sediment flux including the bed porosity p. A uniform grain size and a saturated sediment transport are the main hypotheses of this formulation. The suspended sediment flux is neglected in this model, according to the criteria proposed by [*Van Rijn*, 1989]. This criteria states that no sediment is transported by suspension if the sediment fall velocity is greater than the friction velocity. For a 500 μm sediment diameter, a 1 m s^{-1} current in 30 m of water depth, the fall velocity is equal to 0.07 m s^{-1} whereas the friction velocity is equal to 0.03 m s^{-1}.

[15] The bed load sediment flux $\vec{S}_b$ is parameterized by a generic formula based on the Meyer-Peter Muller model

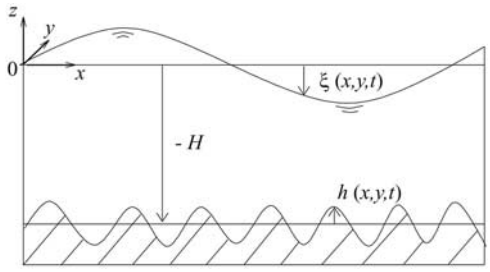

Figure 1. Sketch of the model geometry and related variables.

[*Van Rijn*, 1989] and including a bottom slope effect term to take into account gravity driven sediment transport,

$$\vec{S}_b = \alpha \parallel \vec{u} \parallel^3 \left(\frac{\vec{u}}{\parallel \vec{u} \parallel} - \lambda \vec{\nabla} h \right), \tag{2}$$

with λ the bottom slope effect coefficient ($1 \leq \lambda \leq 3$). Including the bed porosity p, the efficiency factor α is computed from [*Van Rijn*, 1989]

$$\alpha = \frac{1}{1-p} \frac{8\sqrt{g}}{(s-1)C_h^3}, \tag{3}$$

with $s = \rho_{sediment}/\rho_{water}$ and C_h the Chézy coefficient modeled by

$$C_h = 18 \log\left(\frac{12(H+\xi-h)}{3d_{50}} \right), \tag{4}$$

with d_{50} the grain size.

[16] The bottom level is fixed at the upstream boundary whereas no boundary condition is needed at the downstream boundary as the sediment wave propagates downstream. A null sediment flux is imposed at wall boundaries. The numerical resolution of equation (1) relies on the Sisyphe software [*Peltier and Latteux*, 1995] based on a finite element semi-implicit temporal scheme [*Peltier et al.*, 1991].

2.2. Hydrodynamic Model

[17] Two different sets of equations are used for the computation of the hydrodynamic variables. The first one is based on the stationary shallow-water equations valid in the long wave approximation. The second one is a simplified version of the first one, called the continuity correction, valid as long as the bottom evolution remains small.

2.2.1. Stationary Shallow-Water Model (SWM)

[18] The depth-integrated velocity field $\vec{u} = (u, v)$ and the free-surface elevation (ξ) are computed according to the conservation of momentum and mass,

$$u\frac{\partial u}{\partial x} + v\frac{\partial u}{\partial y} = -g\frac{\partial \xi}{\partial x} - \frac{1}{\rho(H+\xi-h)}\tau_x + \nu_e \Delta u, \tag{5}$$

$$u\frac{\partial v}{\partial x} + v\frac{\partial v}{\partial y} = -g\frac{\partial \xi}{\partial y} - \frac{1}{\rho(H+\xi-h)}\tau_y + \nu_e \Delta v, \tag{6}$$

$$\frac{\partial}{\partial x}[(H+\xi-h)u] + \frac{\partial}{\partial y}[(H+\xi-h)v] = 0, \tag{7}$$

where g is the gravity acceleration and ν_e the effective viscosity (molecular and turbulent). The term τ_x (respectively, τ_y) is the x-component (respectively, y-component) of the bottom friction stress $\vec{\tau}$ which is parameterized by

$$\vec{\tau} = \frac{\rho g}{K^2 (H+\xi-h)^{1/3}} \parallel \vec{u} \parallel \vec{u}, \tag{8}$$

where K is the Strickler coefficient which is related to the Chézy coefficient,

$$C_h = K(H+\xi-h)^{\frac{1}{6}}. \tag{9}$$

[19] Equations (5)–(7) are solved by a finite element method using the Telemac 2D software [*Hervouet and Van Haren*, 1994] which is often used for engineering studies [*Hervouet and Bates*, 2000]. As boundary conditions, a stationary fluid discharge is imposed upstream, a stationary free surface level downstream and a slip condition at the lateral boundaries.

2.2.2. Continuity Correction Model (CCM)

[20] As long as the bottom evolution is small, a simplified model called "continuity correction" can be used [*De Vriend et al.*, 1993b]. This technique, which is based on the assumption that the flow direction is less sensitive to the bed evolution than its magnitude, reads

$$\xi(t_0 + dt) = \xi(t_0) \tag{10}$$

$$\vec{u}(t_0 + dt) = \frac{H+\xi-h(t_0)}{H+\xi-h(t_0+dt)}\vec{u}(t_0), \tag{11}$$

where $\xi(t_0)$ and $\vec{u}(t_0)$ have been computed by either the CCM model or the SWM model.

2.3. Coupling and Computational Time

[21] The ideal coupled model would always use the SWM model to compute the hydrodynamics. However, in order to reduce the computational time, another strategy is used (Figure 2). Each morphodynamical computation begins with one SWM model computation. As long as the bed evolution is small compared to the water depth ($R = [h(t) - h(t_0)]/d \leq R_c$, with d the water depth, t the current time and t_0 the last time the SWM model was used), the CCM model is used at each sedimentary time step. Each time the bottom evolution reaches the critical evolution ratio ($R = R_c$), the hydrodynamics is updated with the SWM model.

3. Bedform Generation

[22] The aim of this section is to analyze the ability of this morphodynamical model to estimate the sand bed stability properties as well as to get some insights into the instability process. In order to validate the model and analyze the stability processes, a linear stability analysis is performed for the temporal evolution of a bottom perturbation subject to a spatially uniform stationary current.

3.1. Linear Stability Analysis

3.1.1. Model Formulation

[23] The linear stability analysis of the morphodynamical model (equations (1)–(8)) is performed along the lines of *Fluit and Hulscher* [2002] with a different bottom friction parameterization, using the same scalings. Although the length and timescales are based on tidal scales, this scaling

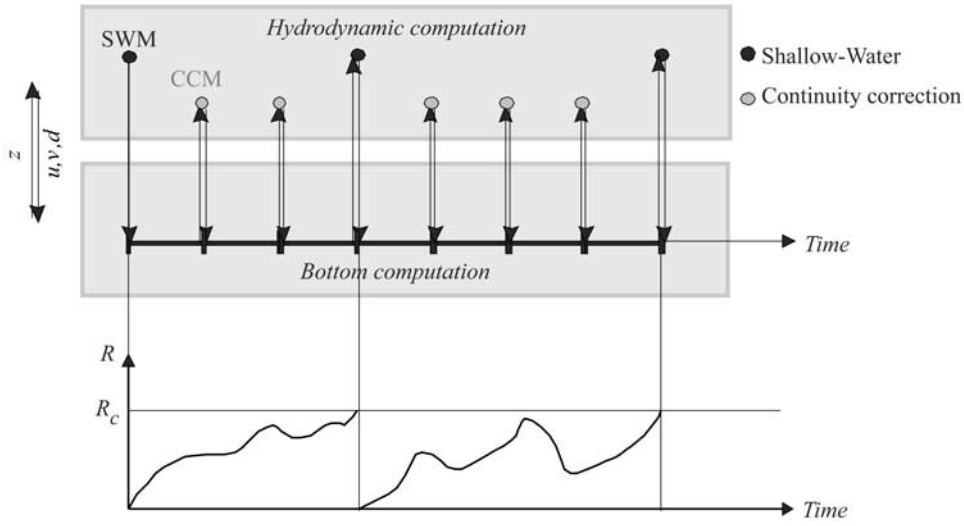

Figure 2. Coupling method.

is also relevant for a quasi-steady current [*Fluit and Hulscher*, 2002].

$$\vec{u} = Uu* \; ; \; \vec{x} = l_m x* \; ; \; t = \frac{t*}{\sigma}; h = Hh* \; ; \; \xi = \frac{Ul_m\sigma}{g}\xi*, \quad (12)$$

with U a magnitude for the mean current, σ a typical tidal frequency (in the North Sea, $\sigma = 1.4 \cdot 10^{-4}$ s^{-1} for the M_2-tide), $l_m = U/\sigma$ the tidal excursion length (about 7142 m for a current of 1 m s^{-1}), g the gravity acceleration, and H the water depth (typically 30 m in the North Sea).

[24] Neglecting the viscous terms and dropping the asterisks for convenience, the dimensionless equations can be written

$$\frac{\partial \xi}{\partial x} + u\frac{\partial u}{\partial x} + v\frac{\partial u}{\partial y} = -\hat{K}\frac{\sqrt{u^2+v^2}}{\left(1+\delta^2\xi-h\right)^{4/3}}u, \quad (13)$$

$$\frac{\partial \xi}{\partial y} + u\frac{\partial v}{\partial x} + v\frac{\partial v}{\partial y} = -\hat{K}\frac{\sqrt{u^2+v^2}}{\left(1+\delta^2\xi-h\right)^{4/3}}v, \quad (14)$$

$$\frac{\partial}{\partial x}\left[\left(1+\delta^2\xi-h\right)u\right] + \frac{\partial}{\partial y}\left[\left(1+\delta^2\xi-h\right)v\right] = 0, \quad (15)$$

$$\frac{\partial h}{\partial t} = -\hat{\alpha}\vec{\nabla}.\parallel\vec{u}\parallel^3\left(\frac{\vec{u}}{\parallel\vec{u}\parallel} - \hat{\lambda}\vec{\nabla}h\right). \quad (16)$$

[25] The dimensionless parameters are defined by

$$\hat{K} = \frac{gU}{K^2\sigma H^{4/3}} \quad (17)$$

$$\hat{\alpha} = \frac{\alpha U^3}{Hl_m\sigma} = \frac{1}{\sigma T_m} \quad (18)$$

$$\hat{\lambda} = \lambda\frac{H\sigma}{U} \quad (19)$$

$$\delta = l_m/L, \quad (20)$$

where $L = \frac{\sqrt{gH}}{\sigma}$ is the tidal wavelength. As δ is small (of the order of 0.01 in the North Sea), the δ^2 terms will be subsequently neglected. T_m is the morphological timescale. This timescale depends on the sediment grain size but in any case is far larger than the hydrodynamic scale (for typical North Sea conditions and d_{50} = 500 microns, T_m = 303 years). Then, a slow time variable $\tau = \hat{\alpha}t$ can be used.

3.1.2. Analytical Solution

[26] The base flow solution is chosen to be $(u_0, v_0, \xi_0, h_0) = (C, 0, -\hat{K}C^2x, 0)$ where C is a constant. The first-order solution satisfies the following equations:

$$\frac{\partial \xi_1}{\partial x} + C\frac{\partial u_1}{\partial x} + \hat{K}\left(2Cu_1 + C^2\frac{4}{3}h_1\right) = 0, \quad (21)$$

$$\frac{\partial \xi_1}{\partial y} + C\frac{\partial v_1}{\partial x} + \hat{K}Cv_1 = 0, \quad (22)$$

$$\frac{\partial u_1}{\partial x} + \frac{\partial v_1}{\partial y} = C\frac{\partial h_1}{\partial x}, \quad (23)$$

$$\frac{\partial h_1}{\partial \tau} = -C^2\left(3\frac{\partial u_1}{\partial x} + \frac{\partial v_1}{\partial y}\right) + \lambda C^3\left(\frac{\partial^2 h_1}{\partial x^2} + \frac{\partial^2 h_1}{\partial y^2}\right). \quad (24)$$

[27] The problem is then solved in the Fourier space for $\tilde{u}_1$ and $\tilde{v}_1$,

$$\tilde{u}_1 = \frac{1}{3}C\frac{\hat{K}(4l^2-3k^2)+3ik^3}{-\hat{K}(k^2+2l^2)+ik(k^2+l^2)}\tilde{h}_1 \quad (25)$$

$$\tilde{v}_1 = \frac{1}{3}Clk\frac{-10\hat{K}+3ik}{-\hat{K}(k^2+2l^2)+ik(k^2+l^2)}\tilde{h}_1, \quad (26)$$

where $\vec{k} = (k, l)$ is the two-dimensional dimensionless wavenumber vector and $i^2 = -1$. The Fourier transform of the bottom perturbation $\tilde{h}_1$ is governed by

$$\frac{\partial \tilde{h}_1}{\partial \tau} = \omega\tilde{h}_1, \quad (27)$$

with the complex frequency ω,

$$\omega = C^3\left[\frac{1}{3}\frac{i\hat{K}k(2l^2-9k^2)-3k^2(3k^2+l^2)}{-\hat{K}(k^2+2l^2)+ik(k^2+l^2)} - \hat{\lambda}\left(k^2+l^2\right)\right]. \quad (28)$$

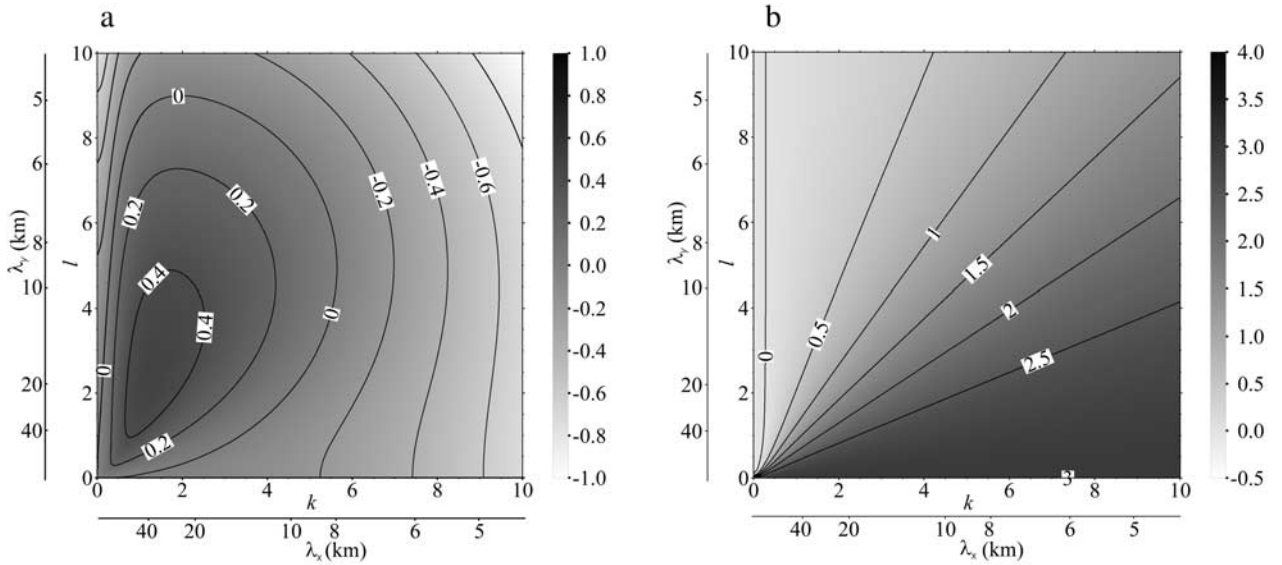

Figure 3. Linear stability analysis. (a) Dimensionless growth rate $Re(\omega)$. (b) Dimensionless phase celerity C_w. Here, λ_x and λ_y are the corresponding wavelengths (km); ($\hat{\lambda} = 7.27 \cdot 10^{-3}$, $\hat{K} = 0.249$, $\hat{\alpha} = 7.46 \cdot 10^{-7}$).

[28] The growth rate $Re(\omega)$ and the phase speed $C_w = \frac{Im(\omega)}{\|\vec{k}\|}$ of the bottom perturbation are

$$Re(\omega) = C^3\left[\frac{2\hat{K}k^2l^2}{3}\cdot\frac{7k^2+4l^2}{\hat{K}^2(k^2+2l^2)^2+k^2(k^2+l^2)^2}-\hat{\lambda}\left(k^2+l^2\right)\right] \tag{29}$$

$$C_w = \frac{C^3k}{3(k^2+l^2)^{1/2}} \frac{-\hat{K}^2(2l^2-9k^2)(k^2+2l^2)+3k^2(3k^2+l^2)(k^2+l^2)^2}{\hat{K}^2(k^2+2l^2)^2+k^2(k^2+l^2)^2}. \tag{30}$$

3.1.3. Results

[29] Typical North Sea values are used for the model parameters: the water-depth $H = 30$ m, the current velocity $U = 1$ m s^{-1}, the sediment grain size $d_{50} = 500$ μm [*van der Molen and de Swart*, 2001], the bed porosity $p = 0.26$ (corresponding to the most stable packing) [*Van Rijn*, 1989]. According to these values, $K = 54.9$ m$^{1/3}$ s^{-1} and $\alpha = 2.24 \cdot 10^{-5}$ s^2 m^{-1}. Assuming a 30° angle of repose for the sediment, the bottom slope effect coefficient $\lambda = 1.7$ is chosen.

[30] The growth rate and the phase celerity are plotted in Figure 3. A band of amplified modes is observed (Figure 3a). The most amplified mode $\vec{k} = (1.3, 2.5)$ has a growth rate of 0.48 for a morphological time $T_m = 303$ years. According to this result, a 1-mm perturbation needs 4366 years to reach an amplitude of 1 m. This mode corresponds to a bed perturbation with an angle of 27.5° between the bottom crests and the main current direction, and a wavenumber of $\|\vec{k}\| = 2.8$ corresponding to a dimensional wavelength of 16 km.

[31] One should notice that if the slope effect is not taken into account, all the modes are unstable (Figure 4). For increasing wavenumber, the crest orientation becomes more parallel to the main flow and the growth rate increases so that the most amplified mode has an infinitely small wavelength. Including the bottom slope effect leads to the selection of the wavelength so that the current controls the bedform direction, whereas the gravity driven sediment flow selects its wavelength. In the linear regime, the gravity effect plays therefore a dominant role.

[32] For a given orientation, all the bedform have the same phase celerity (Figure 3b). This means that the celerity depends on the bedform orientation but not on its wavelength. The most amplified mode has a phase

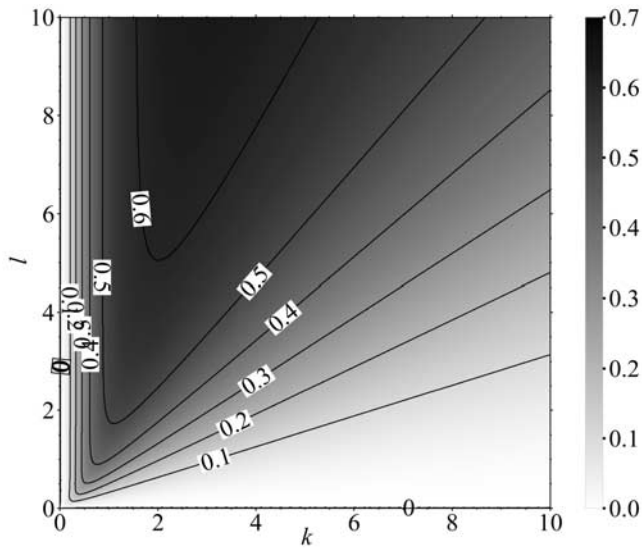

Figure 4. Dimensionless growth rate without bottom slope effect ($\hat{\lambda} = 0$, $\hat{K} = 0.249$, $\hat{\alpha} = 7.46 \cdot 10^{-7}$).

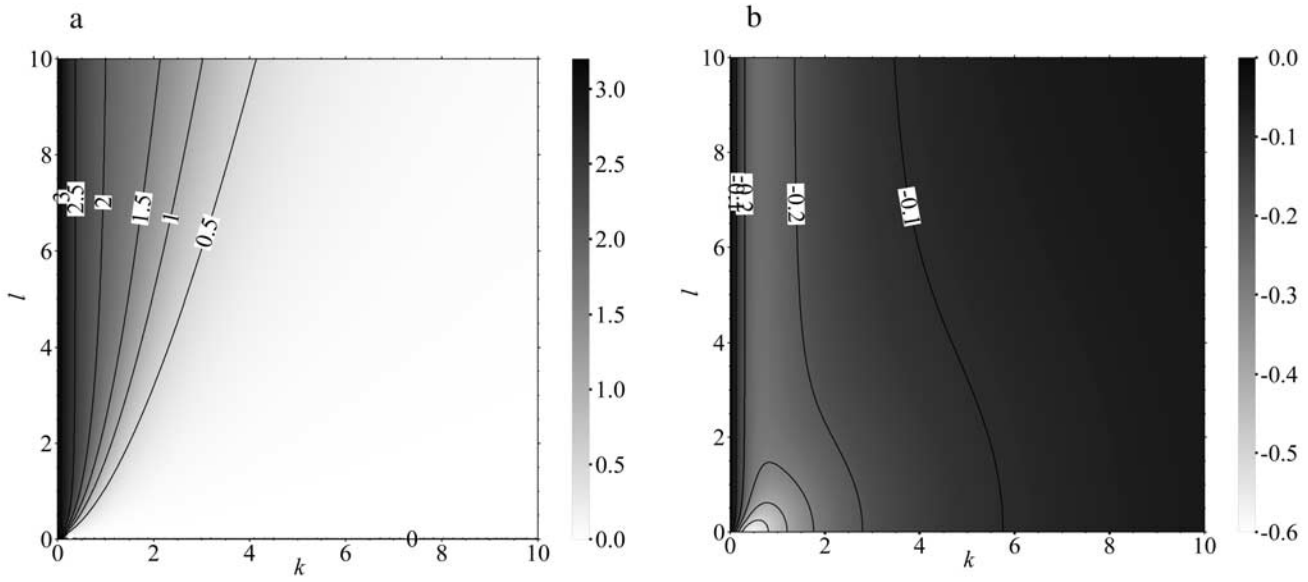

Figure 5. Theoretical phase-lags between velocity and bottom: (a) ϕ_u along the x-direction and (b) ϕ_v along the y-direction.

celerity of 0.595 rd per T_m, that is to say a migration rate of 5 m yr^{-1}.

3.2. Physical Mechanisms of Instability: Current-Bottom Phase-Lag

[33] *Engelund and Fredsoe* [1982] discussed the bottom instability process in terms of the spatial phase-lag between the sediment flux and the bottom perturbation. *Colombini et al.* [1987] extended the analysis to a two-dimensional situation. The same kind of analysis is performed in this section. As the sediment flux is related to the fluid velocity by equation (2), the growth rate of the instability can be related to the phase-lag between the fluid velocity and the bottom perturbation.

[34] Assuming a negligible free surface slope, the fluid velocity can be written as $\vec{u} = (C + u_1, v_1)$. For any sinusoidal small bottom perturbation ($h_1 = |h_1| \cos(kx + ly)$), u_1 (respectively, v_1) is a sinusoidal function with a phase-lag ϕ_u (respectively, ϕ_v) being the phase-lag between the u-component (respectively, v-component) of the fluid velocity and the bottom. From equation (24), after some algebra, we get the following dimensionless equation, dropping the asterisks for convenience:

$$\frac{\partial h_1}{\partial \tau} + \vec{w}.\vec{\nabla} h_1 = \omega' h_1, \tag{31}$$

where

$$\vec{w} = \frac{C^2}{|h_1|}(3|u_1|\cos(\phi_u), |v_1|\cos(\phi_v)) \tag{32}$$

$$\omega' = \frac{C^2}{|h_1|}(3k|u_1|\sin(\phi_u) + l|v_1|\sin(\phi_v)) - C^3\hat{\lambda}(k^2 + l^2). \tag{33}$$

[35] The term $\vec{w}.\vec{\nabla} h_1$ on the left-hand side of equation (31) corresponds to the propagation of the bottom perturbation, whereas the right-hand term is responsible for the growth or the decay of the perturbation. ω' is therefore similar to the growth rate $Re(\omega)$. From equation (33), one can see that ω' is the sum of three terms. The last term, related to the bottom slope effect, is always a damping term. Depending on the phase-lags ϕ_u and ϕ_v, the two other terms can be destabilizing or damping terms. If the phase-lag $0 \leq \phi_u < \pi$ (respectively, ϕ_v), the velocity u_1 (respectively, v_1) has a destabilizing effect; otherwise it has a damping effect.

[36] Using equation (23), we obtain the following relation between the two phase-lags:

$$\sin\phi_v = -\frac{|u_1|}{|v_1|}\frac{k}{l}\sin\phi_u. \tag{34}$$

[37] Thus if the phase-lag ϕ_u is positive, the phase-lag ϕ_v is negative. So, when the phase-lag ϕ_u has a destabilizing effect, ϕ_v has a stabilizing one.

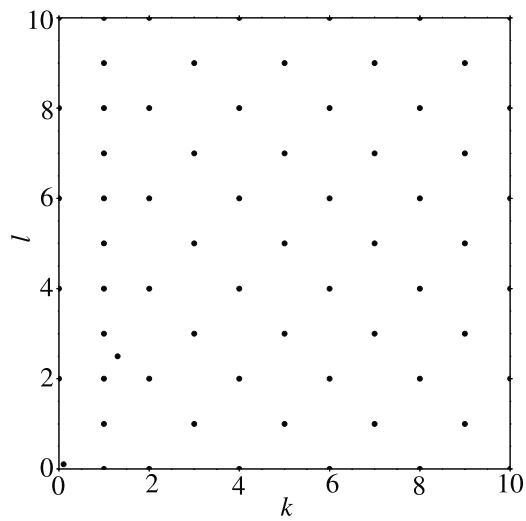

Figure 6. Sampling of the wavevector space. Each point corresponds to a selected mode.

[38] Using equation (34), ω' can be simplified,

$$\omega' = \frac{C^2}{|h_1|} 2k|u_1| \sin(\phi_u) - \hat{\lambda} C^3 \left(k^2 + l^2\right). \tag{35}$$

[39] Therefore, the bottom perturbation will be amplified as long as the longitudinal velocity has a destabilizing effect.

[40] Furthermore, the phase-lags ϕ_u and ϕ_v can be computed from the linear stability analysis results,

$$\begin{aligned}\phi_u &= -\arctan\frac{Im(\tilde{u}_1)}{Re(\tilde{u}_1)} \\ &= -\arctan\left(\frac{\hat{K}kl^2(7k^2+4l^2)}{\hat{K}^2(4l^2-3k^2)(k^2+2l^2)-3k^4(k^2+l^2)}\right)\end{aligned} \tag{36}$$

$$\begin{aligned}\phi_v &= -\arctan\frac{Im(\tilde{v}_1)}{Re(\tilde{v}_1)} \\ &= -\arctan\left(\frac{\hat{K}k(7k^2+2l^2)}{10\hat{K}^2(k^2+2l^2)+3k^2(k^2+l^2)}\right).\end{aligned} \tag{37}$$

[41] In Figure 5, the phase-lags are plotted according to equations (36) and (37). We observe that for the set of parameters considered, the phase-lag ϕ_u is always positive, in the range $[0, \pi]$ and then ϕ_v is always negative, in the range $[0, -\pi]$. Thus, the longitudinal component u_1 has a destabilizing effect whereas the transverse component v_1 has a stabilizing effect.

3.3. Numerical Results

3.3.1. Method

[42] The numerical morphodynamical model is used to compute the dimensionless complex frequency ω over a wavevector subspace defined by dimensional wavenumbers ranging from 0 to 10 in each direction. A sampling of this subspace is performed (Figure 6) and, for each selected mode, the temporal evolution of the corresponding monochromatic infinitesimal bottom perturbation is computed using the numerical model (Figure 7).

[43] The critical bottom evolution ratio R_c should be chosen to optimize the method in terms of computational time and accuracy. For a given mode, two values of the critical ratio R_c have been tested (Figure 8). However, the estimated growth rate are almost similar, despite the fact that for the larger value of R_c, the SWM is only solved once over 1 year. From this test the value $R_c = \infty$ is used in all the computations. These preliminary tests show that the computations should be carried out over a large enough time in order that the growth rate should reach its constant linear regime value (Figure 8). This value is set to 200 days. The growth rate $Re(\omega)$ and the phase celerity C_w are computed from the Fast Fourier Transform of the difference between the final ($h(x, y, 200$ days)) and initial ($h(x, y, 0)$) bottom positions.

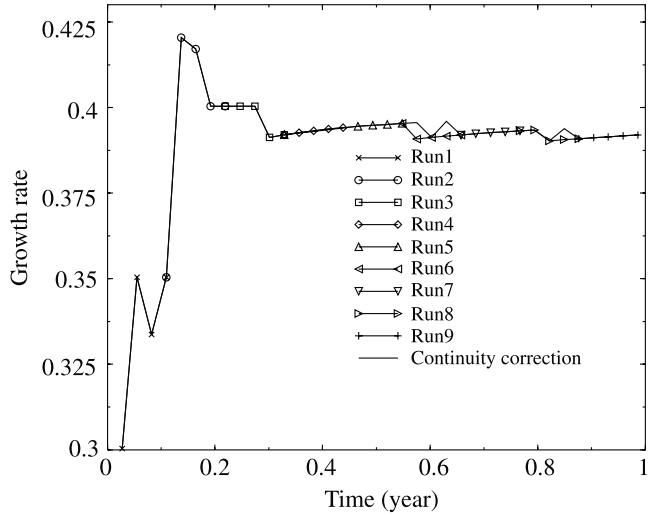

Figure 8. Computed dimensionless growth rate for the $(k, l) = (1.3, 2.5)$ mode versus time for $R_c = 10^{-5}$ (solid line and symbols) and $R_c = \infty$ (dotted line); ($\hat{\lambda} = 7.27 \cdot 10^{-3}$, $\hat{r} = 0.249$, $\hat{\alpha} = 7.46 \cdot 10^{-7}$).

[44] For each computation, the length and width of the computational domain are 4 times the longitudinal and transverse bottom perturbation wavelength (Figure 7). The same number of 32,258 elements is used in the computations so that a same resolution of 32 grid points per bottom wavelength is obtained for all the computed modes. In addition, the hydrodynamic time step used in the iterative procedure to reach the steady state is selected to keep the *CFL* number (proportional to $\frac{\Delta t}{\Delta x}$) constant in each compu-

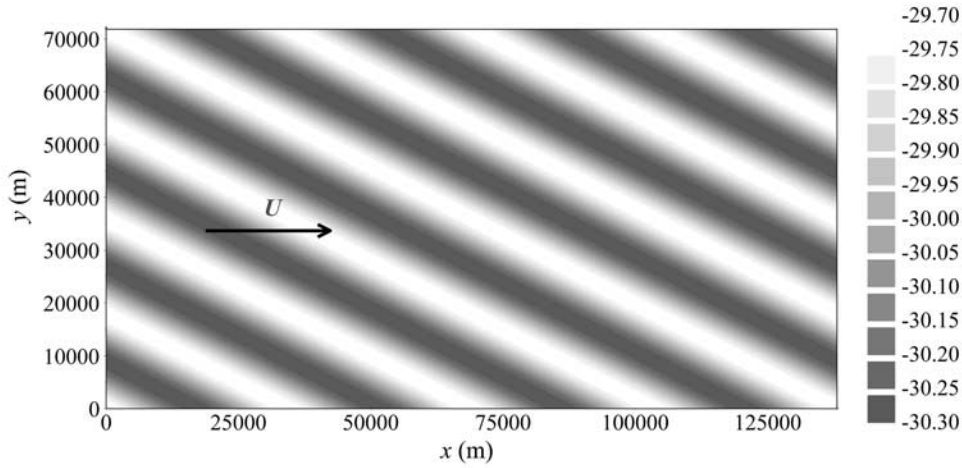

Figure 7. Initial bathymetry (in meters), mode (1.3, 2.5).

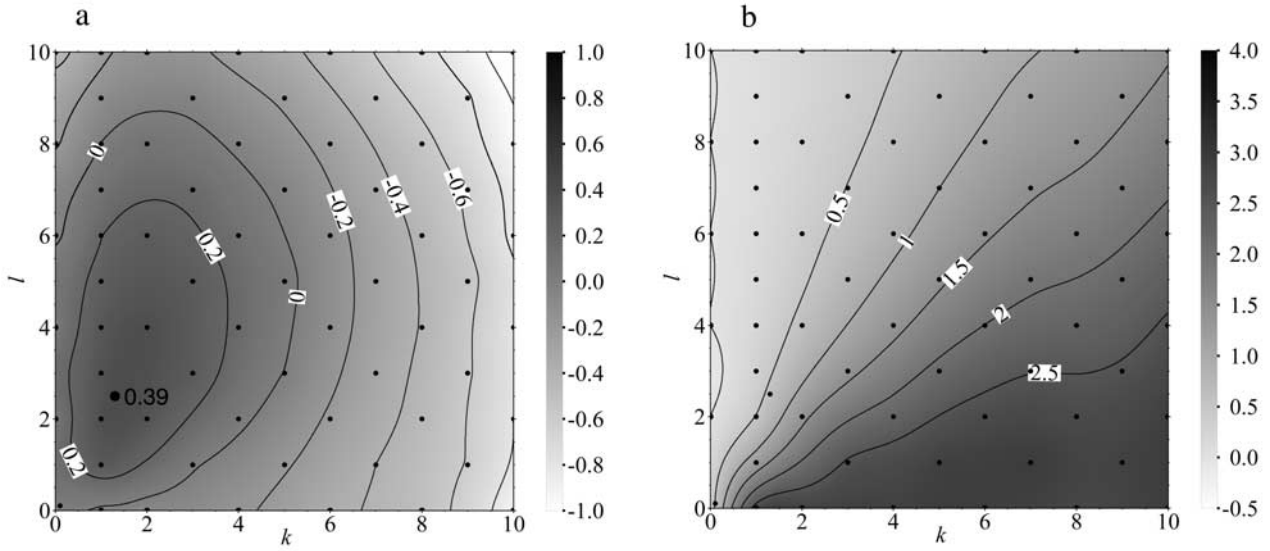

Figure 9. Numerical model results: (a) dimensionless growth rate and (b) dimensionless phase celerity; ($\hat{\lambda} = 7.27 \cdot 10^{-3}$, $\hat{K} = 0.249$, $\hat{\alpha} = 7.46 \cdot 10^{-7}$).

tation. Thanks to the special choice of time step and grid sizes, the numerical truncation errors are expected to be the same for all the computations.

[45] $H = 30$ m, $U = 1$ m s^{-1} are the values used for the hydrodynamic boundary conditions. The parameter values are those already used in the stability analysis. The dimensional effective viscosity is $v_e = 10^{-4}$ m^2 s^{-1}. The dimensional amplitude of the initial perturbation is $h(t = 0) = 30$ cm, that is to say 1% of the water depth H.

3.3.2. Results

[46] The plot of the growth rate estimated by the morphodynamical model (Figure 9a) shows that the results are very similar to those obtained by the stability analysis (Figure 3a) with the same band of amplified modes. The most amplified mode has a wavevector $\vec{k} = (1.3, 2.5)$ and its growth rate is $Re(\omega) = 0.392$. These results show that the computed most amplified mode has the proper geometric features, whereas the growth rate is underestimated by 18% in these computations. These discrepancies will be discussed in the next section. However, this underestimation is not uniform over the wavevector subspace as the neutral curve is almost similar in both approaches.

[47] The phase celerity plots (Figures 3b and 9b) show that the numerical results are in good agreement with the analytical results. Thus, numerical errors which may be responsible for errors in the estimation of the phase speed are small.

3.4. Numerical Model and Stability Properties

[48] Let us investigate the phase-lags and the velocity perturbations computed by the numerical model. In Figures 10 and 11 the phase-lags and modulus of velocity perturbations computed from the numerical results and those from the stability analysis are plotted for several

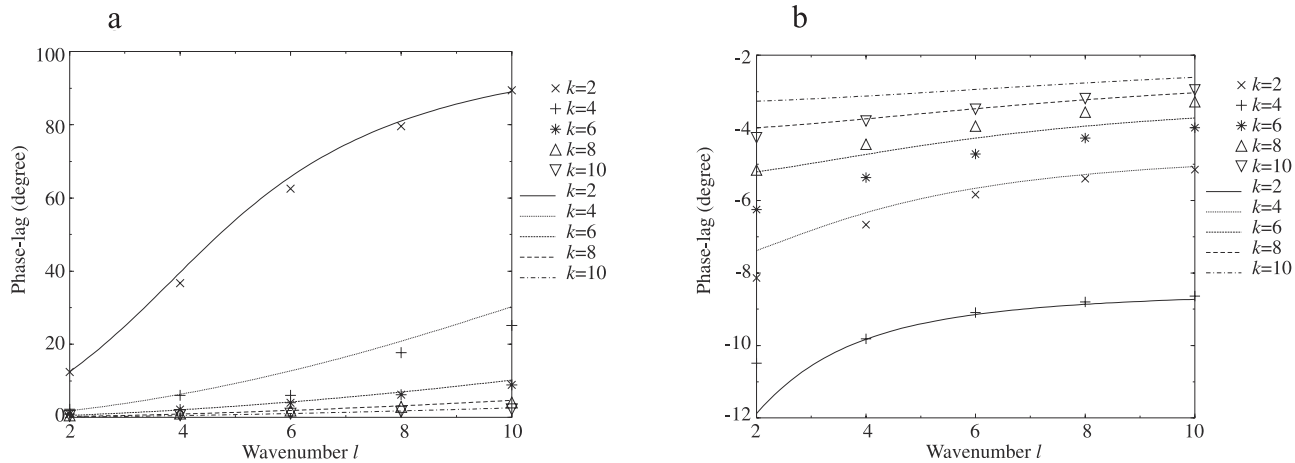

Figure 10. Phase-lags between velocity and bottom (symbols: model, lines: theory): (a) ϕ_u along the x-direction and (b) ϕ_v along the y-direction.

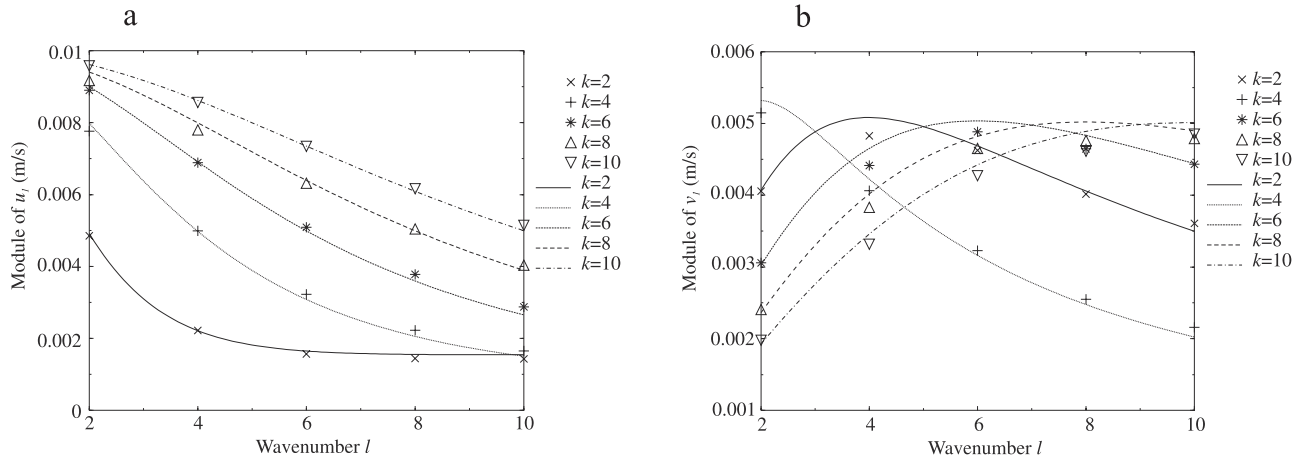

Figure 11. First-order velocity modulus (symbols: model, lines: theory): (a) $|u_1|$ and (b) $|v_1|$.

values of the wavevector components k and l. The numerical phase-lags are in close agreement with the theory for $k = 2$ whereas some discrepancies appear for larger k values (Figure 10). No clear dependence of the error on l is discernible. For $|u_1|$ (Figure 11) the numerical errors are small and almost independent of the mode characteristics. The perturbed transverse velocity modulus $|v_1|$, however, exhibits a behavior similar to those of the phase-lags. If we consider now the most amplified mode (1.3, 2.5), the numerical phase-lags are $\phi_u = 49°$ and $\phi_v = -9.58°$, whereas the theoretical values are $\phi_u = 55°$ and $\phi_v = -13°$. In addition, the modulus are ($|u_1| = 0.0023$ m s^{-1}, $|v_1| = 0.0042$ m s^{-1}) and ($|u_1| = 0.0025$ m s^{-1}, $|v_1| = 0.0046$ m s^{-1}) for the model and the theory, respectively. Therefore, the error on the growth rate induced by the hydrodynamic errors can be estimated from equation (33) to be 17%. Thus the differences between the model and the theoretical growth rate (18%) are almost exclusively due to the hydrodynamic computation whereas the bed evolution model and the coupling scheme appear to contribute only marginally to the error.

[49] Although no parametric study has been performed, an increase in the resolution (number of grid point per wavelength) and in the size of the computational domain would have a positive impact on the growth rate error at the expense of a stronger computational effort. We should also keep in mind that the assumption of a uniform flow in the analytical model is no longer satisfied in the numerical model due to the presence of bottom friction.

4. Finite Amplitude Behavior

[50] The knowledge of the final height of the bottom bedforms generated by the instability like sandbanks is very desirable for practical applications and cannot be estimated by a linear theory. Then, an attempt is made to estimate the saturation height of tidal sandbanks submitted to symmetrical block-function currents and to investigate the mechanisms involved in the saturation process.

4.1. Estimation of Saturation Height

[51] Although possible in principle, the computation of the time evolution of a small bottom perturbation with the numerical model until saturation is practically irrelevant since the timescale of the bottom instability (of the order of T_m) would require years of computer time. However, the morphodynamical model can be used to get some insights into the saturation process of these sandbanks provided some assumptions are made. A technique has thus been developed to estimate the saturation height of an amplified mode.

4.1.1. Hypothesis and Method

[52] As the scales of the amplified modes are close to those of sandbanks and as the slopes of real sandbanks are less than 6° [*Stride*, 1982], the two-dimensional depth integrated morphological model is suitable to study the saturation of the tidal sandbanks.

[53] The main underlying assumption of the proposed technique to estimate the saturation height is that only one unstable mode will survive at finite amplitude, so that the studied bedform will be sinusoidal. In other words, the only nonlinear interaction taken into account is the self interaction leading to saturation. The choice of this symmetrical shape is consistent with the fact that although real sandbanks exhibits a slight asymmetry, symmetrical tidal currents may produce symmetrical saturated bedforms.

[54] It has been shown that the scales and the orientation of the linearly most unstable mode are close to those of real sandbanks [*Huthnance*, 1982; *Fluit and Hulscher*, 2002]. In addition, previous studies have shown that the most unstable mode may dominate at finite amplitude [*Calvete et al.*, 2001; *Hibma et al.*, 2001]. Thus, we assume that the linearly most amplified mode will be the surviving mode at finite amplitude. The sensitivity of the results to the exact shape of the symmetrical saturated sandbanks will also be investigated.

[55] The only relevant quantity to be estimated in the proposed technique is the finite amplitude growth rate. Linear stability analysis results [*Fluit and Hulscher*, 2002] show that the growth rate is the same for a bottom submitted to a block-function alternate current (a simple model for a tidal current) and for a steady current. We performed also some numerical computations where the growth rates of the most amplified mode have been computed for different values of the finite amplitude initial height and proved to

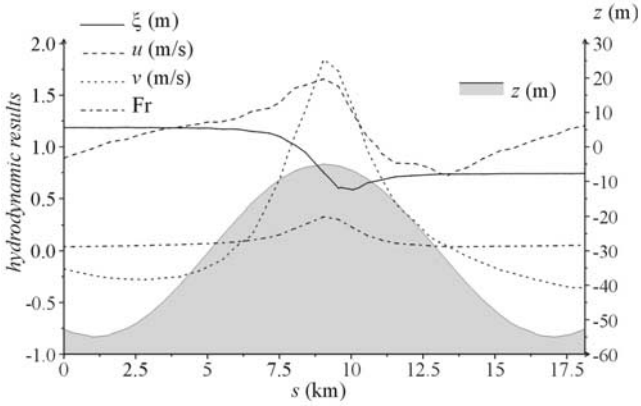

Figure 12. Cross-section of free surface $\xi(s)$, velocity (u, v) and Froude number Fr for a bedform amplitude $h = 25$ m of the linearly most amplified mode $(k, l) = (1.3, 2.5)$; s is the coordinate along this direction.

be the same for both kinds of currents. The morphological phase velocity is, however, equal to zero for alternate current only. Thus, as the computational time is significantly larger for the block-function current than for the steady one, the computations are performed for a steady current. The results hold for alternate currents as well and are analyzed from this perspective. Obviously, the symmetrical sinusoidal shape will hardly be an asymptotic solution for a uniform current which are only used here for convenience.

[56] To estimate the saturation height of the sandbanks, the growth rate of the linearly most amplified mode is computed for increasing values of the height of the bottom perturbation. A positive growth rate means that the perturbation is still growing; that is to say, the saturation height is larger than the considered perturbation height. An opposite conclusion has to be drawn if the growth rate is negative. For each computation, the dimensionless amplification rate is computed between $t = 0$ and $t = 200$ days. For all the computations, the flow is subcritical (Froude number $U/\sqrt{gd}$ lower than 1, Figure 12).

4.1.2. Results

[57] The growth rates are plotted in Figure 13a for different values of the bottom slope effect coefficient $\hat{\lambda}$. In a first stage ($h < 17.5$ m), the growth rate increases until it reaches a maximum which is equal to the linear stability growth rate. This increase should be related to the numerical precision of the hydrodynamic computations as it has been already discussed. In a second stage, the growth rate decreases with increasing initial heights, becoming negative for the highest perturbations (Figure 13). The saturation amplitude is estimated to be $h_s = 24.2$ m for a bottom slope effect $\hat{\lambda}$ of $7.27 \cdot 10^{-3}$, that is to say a dimensionless amplitude $\frac{h_s}{H} = 80.7\%$. The influence of the bottom slope coefficient on the saturation height which decays with increasing $\hat{\lambda}$ is observed to be small.

4.2. Physical Mechanisms of Saturation

[58] The bottom evolution equation (1) may be written,

$$\frac{1}{\alpha}\frac{\partial h}{\partial t} = -\frac{\partial (u^2+v^2)u}{\partial x} - \frac{\partial (u^2+v^2)v}{\partial y} + \lambda \frac{\partial}{\partial x}\cdot\left(\|\vec{u}\|^3 \frac{\partial h}{\partial x}\right) + \lambda \frac{\partial}{\partial y}\left(\|\vec{u}\|^3 \frac{\partial h}{\partial y}\right). \quad (38)$$

[59] The first two terms on the right-hand side (F_x, F_y) are called friction terms, the two others are the bottom slope effects terms (B_x, B_y).

[60] In order to clarify the contributions of the various terms to the dynamics of a fully developed bedform, the maximum values over the physical space of F_x, F_y, B_x and B_y are estimated from the numerical computation of the linearly most amplified mode. For an initial bedform amplitude $h_0 = 25$ m which is larger than the saturation amplitude, $|F_x| = 5.85 \cdot 10^{-3}$ m^2 s^{-3}, $|F_y| = 15.8 \cdot 10^{-3}$ m^2

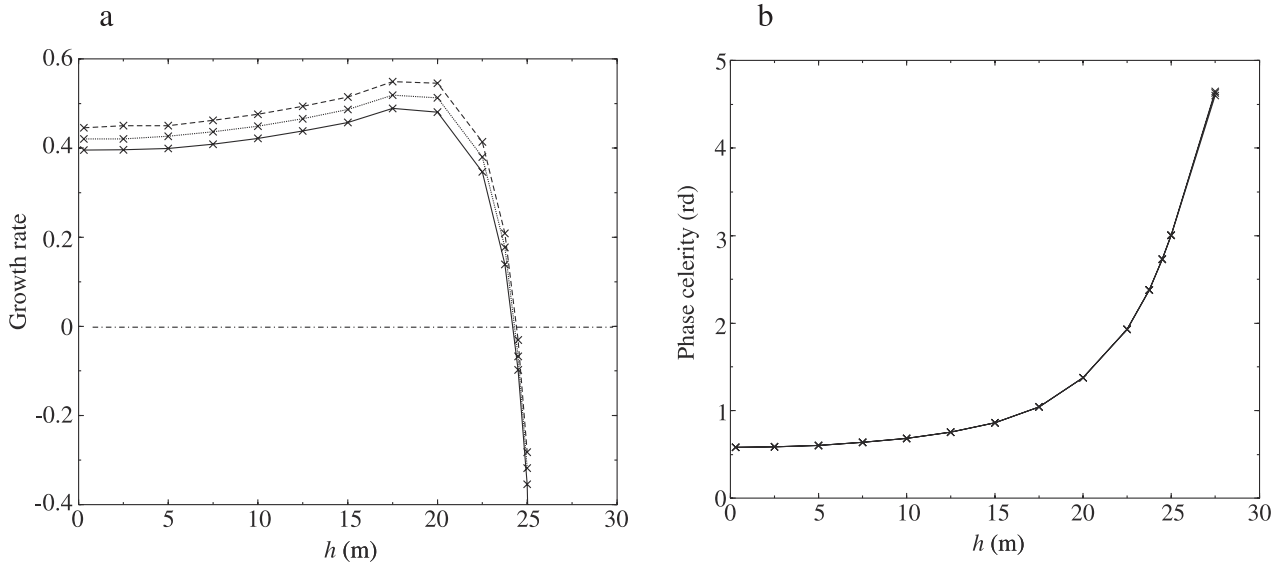

Figure 13. (a) Finite amplitude dimensionless growth rate and (b) phase celerity versus initial bed perturbation amplitude for different values of the bottom slope effect coefficient; $\hat{\lambda} = 7.27 \cdot 10^{-3}$ (solid line), $\hat{\lambda} = 3.64 \cdot 10^{-3}$ (dotted line), $\hat{\lambda} = 0$ (dashed line), and ($\hat{K} = 0.249$, $\hat{\alpha} = 7.46 \cdot 10^{-7}$).

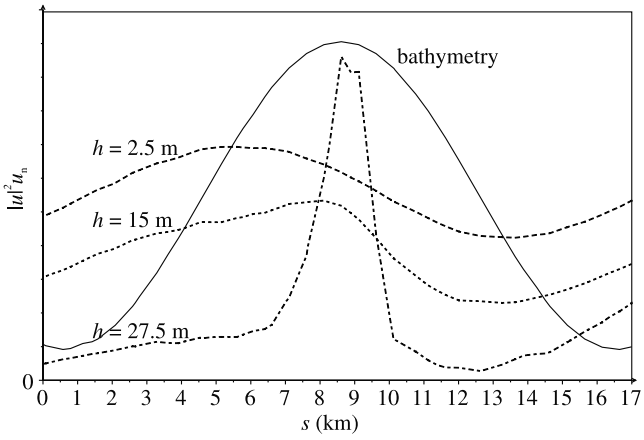

Figure 14. Cross-section of $|u|^2u_n(s)$, perpendicular to the crest, for different initial bottom perturbation amplitudes. The solid line is the bathymetry, u_n is the velocity component normal to the crest, and s is the coordinate along this direction.

s^{-3}, $B_x = 1.58 \cdot 10^{-8}$ m^2 s^{-3}, and $B_y = 10.9 \cdot 10^{-8}$ m^2 s^{-3}. The bottom slope effect terms are several orders of magnitude smaller than the friction terms and are thus of secondary importance in the saturation process which seems to be related to the friction terms.

[61] The term $|u^2|u_n$ (with u_n the velocity normal to the bedform) is proportional to the sediment flux along a direction perpendicular to the crest. A cross-section of this quantity (Figure 14) shows that the phase-lag between the sediment flux maximum and the crest depends on the bedform amplitude. The maximum of the sediment flux moves downstream with increasing height, so that, for high enough bedforms (h = 27.5 m in Figure 14), this maximum is located slightly downwards the crest. From equation (1), a decrease in the crest level should occur.

[62] Furthermore, the fact that even without any bottom slope effect, the finite amplitude bedform saturates confirms that the saturation process is mainly due to an hydrodynamic process and not to the bottom slope effect.

4.3. Shape Influence on the Fully Developed Amplitude

[63] Due to some nonlinear interactions, the saturated bedform may not keep its sinusoidal shape. Thus, in order to estimate the influence of the shape on the saturation height, the same technique has been used to compute the equilibrium height of a symmetrical but not sinusoidal bedform. This bedform is built using the same mode (1.3, 2.5) to which the three first harmonics with an amplitude of 10% of the amplitude of the fundamental are added (Figure 15 shows a bottom cross section perpendicular to the crest). For this shape, the estimated equilibrium amplitude is equal to 24.5 m. There is therefore only a 1% difference between the two bottom shapes. Thus, for symmetrical bedforms, the equilibrium height seems to depend only weakly on the shape.

4.4. Temporal Evolution of a Single Mode Bedform

4.4.1. Amplitude Equation

[64] Equation (27) models the amplification of small-amplitude bottom perturbations. In order to investigate their finite amplitude behavior, this equation requires other terms to limit the amplification. At the lowest order, the Landau equation which allows an exponential growth and a saturation of the amplitude $|\tilde{h}_1|$ by a cubic nonlinearity may be used,

$$\frac{\partial \tilde{h}_1}{\partial \tau} = \omega \tilde{h}_1 - \Phi |\tilde{h}_1|^2 \tilde{h}_1, \tag{39}$$

with ω and Φ dimensionless complex parameters. *Colombini et al.* [1987] proved the relevance of this equation for a similar problem (i.e., alternate bars in rivers). The underlying hypothesis is that nonlinear interactions between the fundamental and other bottom modes are neglected.

[65] Here we restrict ourselves to the real Landau equation as we mainly focus on the height of the sandbanks,

$$\frac{\partial |\tilde{h}_1|}{\partial \tau} = Re(\omega_*) |\tilde{h}_1| - Re(\Phi) |\tilde{h}_1|^3, \tag{40}$$

with $Re(\Phi) = Re(\omega)/|\tilde{h}_1(\infty)|^2$, $\tilde{h}_1(\infty)$ being the saturated amplitude. This equation has already been used to investigate finite amplitude sand waves [*Knaapen et al.*, 2002].

4.4.2. Results

[66] Equation (40) is used to estimate the temporal evolution of the most amplified mode (Figure 16). The estimated linear growth rate and saturation height are used to compute $Re(\omega) = 0.392$ and $Re(\Phi) = 0.602$. Starting from a bedform amplitude equal to the grain size d_{50} = 500 μm and under the assumption that the hydrodynamic conditions remain constant during the life of the bedform, the sinusoidal bottom perturbation needs almost 8000 years to reach its equilibrium amplitude h_s/H of 81% of the undisturbed water depth H, i.e., a height ($2h_s$) from the trough to the crest equal to 48.4 m in 54.2 m of the water depth d.

4.5. Comparison With Real Sandbanks

[67] In order to compare the results obtained in this study to field data, some sandbanks whose sedimentary and hydrodynamic environments resemble those of the numer-

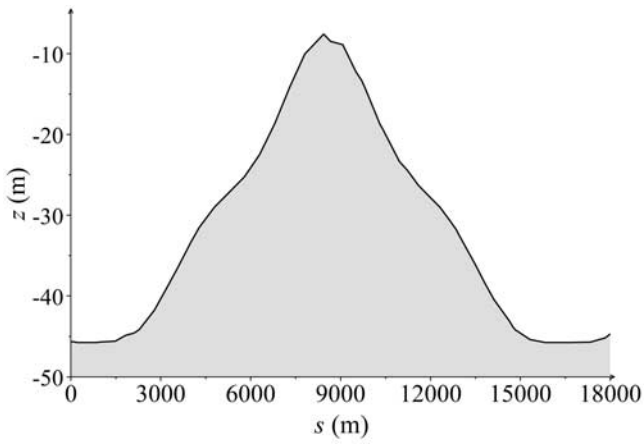

Figure 15. Bathymetric cross-section perpendicular to the crest. The bedform is composed of four modes: (k, l) = (1.3, 2.5) and its three first harmonics; s is the coordinate along this direction.

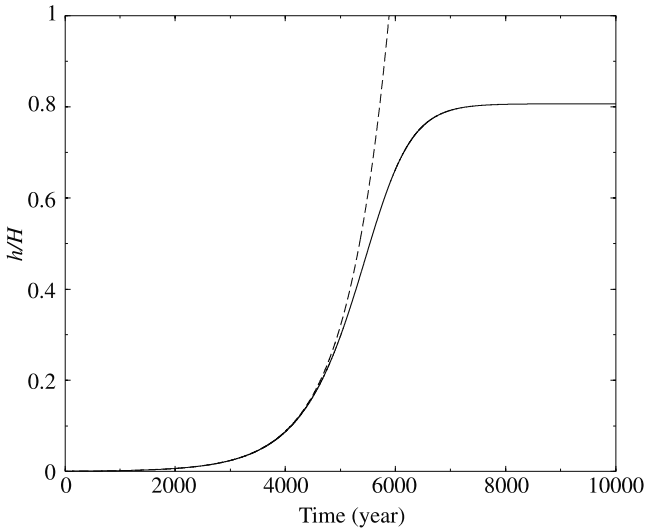

Figure 16. Temporal evolution of the dimensionless sandbank amplitude h/H using the Landau solution (solid line) and the linear stability solution (dashed line). The initial amplitude h is equal to 500 μm, ($\hat{\lambda} = 7.27 \cdot 10^{-3}$, $\hat{K} = 0.249$, and $\hat{\alpha} = 7.46 \cdot 10^{-7}$).

ical computations should be selected. In particular, the sandbanks should be surrounded by sandy areas and oriented with an angle of almost 27° with respect to the mean tidal current direction whereas the mean flow intensity should be about 1 m s^{-1}. Several sandbanks of the North Sea and the English Channel satisfy these criteria (Table 1).

4.5.1. Saturation Amplitude

[68] The relative amplitude of these sandbanks ranges from 56% and 71%. Taking into account the slow evolution of finite amplitude sandbanks, and that the oldest bathymetric data are only a few centuries old, it is not possible to know if the sandbanks have reached their saturated state. Furthermore, the short-term climate variability make the analysis of the dynamics of the present days sandbanks complicated. However, in order to assess the validity of the numerical results, we assume that present-day relative amplitude (56%–71%) is the lower bound for their saturation amplitude.

[69] With a relative amplitude of 81%, the numerical model seems to provide a reasonable estimation for sandbanks saturation amplitude which is however overestimated. We can conclude from this result that the physical processes included in this morphodynamical model seems to be relevant for the finite amplitude dynamics of sandbanks. The overestimation may be due to various factors. Some physical processes not included in the model may play a significant role. Among them, the short surface waves and the occurrence of storms could reduce the height of the large-scale bottom patterns [*Langhorne*, 1982]. No suspended sediment transport has been taken into account in the model. However, this mechanism has been proposed to explain the saturation of sand waves [*Flemming*, 2000]. From the computational results, the friction velocity at the crests of the saturated bedforms is estimated to be 15 m s^{-1}, larger than the fall velocity (0.07 m s^{-1}). Thus, according to the Van Rijn criteria, suspension may play a role. Sandbanks may also be covered by sand waves (Figure 17), which are not taken into account in the model. We should also mention that no attempt has been made to improve the agreement with the observed sandbanks heights using the α, λ and K coefficients.

4.5.2. Saturation Time

[70] During the Holocene sea level rise, the locations of these sandbanks have been flooded between 8300 and 7800 years before present [*Jelgersma*, 1979]. This gives an upper bound for the age of the banks. The age of these sedimentary structures cannot be determined directly. However, the sediment particles can be dated. In the South of North-Sea, there are three different types of sediment: gravel, sand, and shelled fragments. Gravel is dated from the beginning of Holocene sea level rise [*Veenstra*, 1969]. Sand comes from Rhine sands deposits during the lower sea level periods of the Pleistocene [*Houbolt*, 1968]. Shelled fragments are present-time sediments. The sand is the oldest sediment (older than the mean sea level rise). However, as it comes from rivers, it had the chance to reach its present location only when these areas were flooded. Furthermore, from carbonate analysis of a boring in the West Hinder sand ridge, [*Spaink*, 1963] concluded that the sediment has been laid down in a relatively short period during the Holocene age. Thus, it can be concluded that the North Sea sandbanks are about 8000 years old. Since the computed saturation time (8000 years) is very close to the upper bound for real sandbanks age, the numerical model proved to capture properly the temporal dynamics of the instability phenomena.

4.5.3. Migration Rate

[71] Due to the slow evolution of sandbanks, there are few data on the migration rate of these structures. Whereas the Norfolk Banks [*Caston*, 1972] moved toward the northeast direction by about 300 to 600 m during the last century, the Flemish Banks have only slightly moved during the last 300 years [*Eisma et al.*, 1997] and the Hinder Banks seems to be stationary for the past 40 years. These various migration rates should be related to the intensity of steady currents. The growth rate and phase celerity computed for finite amplitudes have been obtained using a steady velocity. Thus, even if this celerity should be zero for symmetrical alternate currents, some information about the migration rate due to either residual currents or wind-induced currents can be gained from the numerical results. The phase-celerity plotted in Figure 13b is an increasing function of the bedform height. At the saturation height, the phase celerity is equal to 1.35 rd per T_m, that is to say, a migration velocity of 11 m yr^{-1} for a steady current of

Table 1. Tidal Sandbanks Characteristics[a]

Area	Water Depth, m	Bank Height h', m	h_*
Schole (English Channel)	50	40	0.66
Casquet (English Channel)	36	29	0.67
Sandettie (North Sea)	30	25	0.71
Southfalls (North Sea)	30	25	0.71
Out Ruytingen (North Sea)	20	16.4	0.70
Noord Hinder (North Sea)	30	21.5	0.56

[a]Data are issued from marine charts and bathymetric data. The dimensionless amplitude h_* is the ratio of the sandbank amplitude ($0.5h'$) divided by the undisturbed sea-bed level ($d - 0.5h'$).

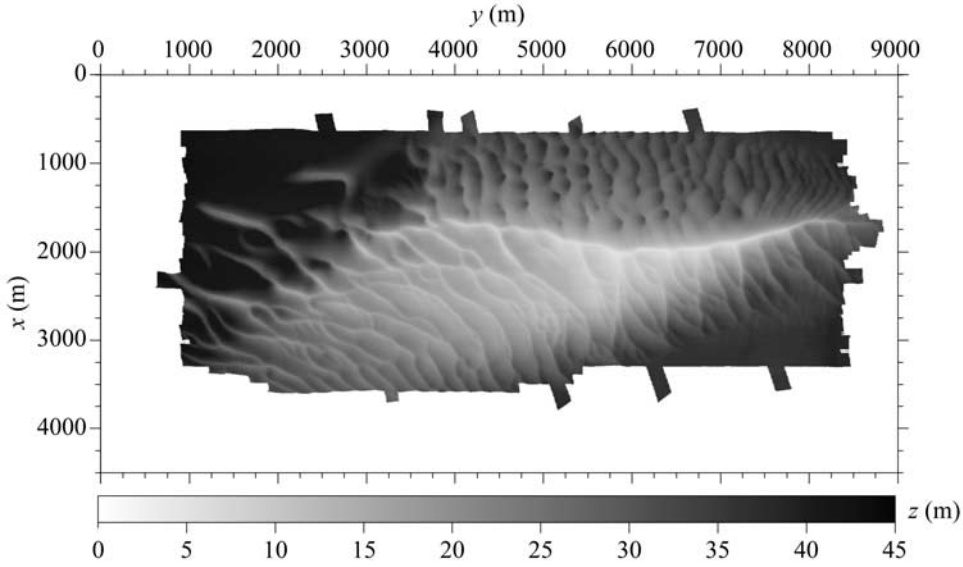

Figure 17. Multibeam echosonder bathymetry of the Schole sandbank (English Channel) (by courtesy of SHOM). The origin for water depth is the hydrographic reference level. The sandbank is covered with sand waves.

1 m s^{-1}. This value is of the same order as the migration rate of the Norfolk Banks (i.e., 3 to 6 m yr^{-1}). Using the morphodynamical model, the sandbanks migration rate can be estimated provided some information on the steady currents over the area available.

5. Conclusion

[72] In this paper, the linear and nonlinear behavior of large-scale sedimentary bedforms like sandbanks have been studied using linear stability analysis and numerical modeling. The main goals were to analyze the sedimentary bottom instability process, to assess the ability of a morphodynamical model, to accurately compute the linear regime, and to gain some insights in the nonlinear sandbanks dynamics.

[73] A simple morphodynamical model including the basic mechanisms for the generation of such bedforms has been considered. Following previous studies, the model is based on bed load transport and depth-integrated hydrodynamic equations including a quadratic friction law.

[74] Using the same equations, a linear stability analysis has been performed for a flat bottom subject to a steady current. A band of long wavelength unstable modes is observed. The orientation of the most amplified mode is controlled by the current driven sediment flux, whereas its wavelength is selected by the gravity driven sediment flux. For a water depth of 30 m, a velocity of 1 m s^{-1} and a grain size of 500 μm, the most amplified mode has a wavelength of about 16 km and its crest is inclined of about 27° with respect to the current direction. The analysis of the spatial phase-lag between the fluid velocity and the bottom perturbation shows that the instability lies in the velocity component in the longitudinal direction whereas the transverse component has a damping effect as well as the bottom slope effect term.

[75] Even if the numerical morphodynamical model seems to underestimate the growth rate of the most unstable mode because of some numerical hydrodynamic inaccuracies, the most amplified mode wavevector is accurately predicted. The good agreement with the theoretical linear stability properties shows that this morphodynamical model can be used for bottom stability analysis.

[76] Then the finite amplitude behavior of the linearly most amplified mode has been studied for a simple tidal flow. The property that the growth rates for the block-function and steady currents are the same is used to extrapolate the results obtained with a steady current to the case of a simple tidal flow. It is moreover assumed that the finite amplitude mode has a symmetrical sinusoidal shape and that the nonlinear interactions between the various modes are neglected.

[77] The saturation amplitude of this mode has been estimated to be 81% of the undisturbed water depth. The bottom slope effect term in the sediment transport formula proved to be several orders of magnitude smaller than the friction terms. Thus, the gravity driven sediment flow cannot be held responsible of the saturation of large-scale bedforms like sandbanks, although it slightly influences the saturation height. From the numerical results, the coefficients of a Landau equation have been computed. This equation has been used to compute the temporal evolution of bottom perturbations until saturation.

[78] Compared with English Channel and North Sea field data, the saturation time seems to be in good agreement whereas the saturation height seems to be slightly overestimated. Some processes not included in the model might play a role in the saturation process. The migration rate due to the steady component of the current has also been estimated and appears to be reasonable.

[79] These results also show that morphodynamical numerical modeling, despite the limitations due to the large

computational resources needed, may provide some interesting insights into the dynamics of bedforms.

Notation

α efficiency factor in the bed-load formula ($s^2\ m^{-1}$).
$\vec{B}$ bottom slope vector ($m^2\ s^{-3}$).
C dimensionless current magnitude.
C_h Chézy coefficient ($m^{1/2}\ s^{-1}$).
C_w phase celerity (s^{-1}).
λ bottom slope effect coefficient.
d water depth (m).
d_{50} grain size (m).
$\vec{F}$ friction vector ($m^3\ s^{-3}$).
g gravity acceleration ($m\ s^{-2}$).
h bed position with respect to the undisturbed bed level ($z = -H$)5 (m).
h' bedform height from trough to crest (m).
h_1 first order bottom perturbation amplitude (m).
h_s saturation amplitude (m).
H undisturbed bed level (m).
$\vec{k}$ dimensionless wavevector (m^{-1}).
K Strickler coefficient ($m^{1/3}\ s^{-1}$).
l_m tidal excursion length (U/σ) (m).
ω complex growth rate (s^{-1}).
p bed porosity.
ϕ_u phase-lag between the velocity component u and the bottom (rd).
ϕ_v phase-lag between the velocity component v and the bottom (rd).
Φ complex damping coefficient.
R bottom evolution ratio.
$\vec{S}_b$ bed load sediment flux ($m^2\ s^{-2}$).
σ tidal frequency (s^{-1}).
t time (s).
T_m morphological timescale (s).
τ slow time $t/(\sigma\ \hat{\alpha})$ (s).
$\vec{\tau}$ bottom friction stress ($kg\ m^{-1}\ s^{-2}$).
$\vec{u}$ depth-integrated velocity vector (u, v) ($m\ s^{-1}$).
U current magnitude ($m\ s^{-1}$).
$\vec{u}_1$ first order velocity vector ($m\ s^{-1}$).
ν_e effective viscosity (molecular and turbulent) ($m^2\ s^{-1}$).
ξ free-surface elevation (m).
x longitudinal coordinate (m).
y transverse coordinate (m).

[80] **Acknowledgments.** The authors would like to thank S.J.M.H. Hulscher of the University of Twente for stimulating discussions and for providing the paper by *Fluit and Hulscher* [2002] prior to publication and V. Guimet from CS-SI for fruitful discussions. We also thank T. Garlan and A. Ehrhold from SHOM for providing field data and the anonymous reviewers for their useful comments. The financial support from SHOM and CNRS is gratefully acknowledged.

References

Blondeaux, P., Mechanics of coastal forms, *Ann. Rev. Fluid Mech.*, *33*, 339–370, 2001.

Blondeaux, P., M. Brocchini, and G. Vittori, A model for sandwaves generation, in *Proceedings of the Marine Sandwave Dynamics Workshop*, edited by A. Trentesaux and T. Garlan, pp. 29–35, Serv. Hydrogr. et Oceanogr. de la Mar., Lille, France, March 2000.

Calvete, D., A. Falques, H. E. de Swart, and N. Dodd, Non-linear modelling of shoreface-connected sandridges, in *Proceedings of Coastal Sediments 1999*, edited by N. C. Kraus and W. G. McDougal, pp. 1123–1138, Am. Soc. of Civ. Eng., Reston, Va., 1999.

Calvete, D., M. Walgreen, H. E. de Swart, and A. Falques, A model for sandridges on the shelf: Effect of tidal and steady currents, *J. Geophys. Res.*, *106*, 9311–9325, 2001.

Caston, V. N. D., Linear sand banks in the southern North Sea, *Sedimentology*, *18*, 63–78, 1972.

Colombini, M., G. Seminara, and M. Tubino, Finite-amplitude alternate bars, *J. Fluid. Mech.*, *181*, 213–232, 1987.

De Vriend, H. J., J. Zyserman, J. Nicholson, J. A. Roelvink, P. Pechon, and H. N. Southgate, Medium-term 2DH coastal area modeling, *Coastal Eng.*, *21*, 193–224, 1993a.

De Vriend, H. J., M. Capobianco, T. Chesher, H. E. de Swart, B. Latteux, and M. J. F. Stive, Approaches to long-term modeling of coastal morphology: A review, *Coastal Eng.*, *21*, 225–269, 1993b.

Dyer, K. R., and D. A. Huntley, The origin, classification and modeling of sand banks and ridges, *Cont. Shelf Res.*, *19*, 1285–1330, 1999.

Eisma, D., J. H. F. Jansen, and T. C. E. van Weering, Sea-floor morphology and recent sediment movement in the North Sea, *Acta Universitatis Upsaliensis: Symposium Universitatis Upsaliensis Annum Quiongentesimum Celebrantis, 2*, edited by E. Oele, R. T. E. Schuttenhelm, and A. J. Wiggers, pp. 217–231, Acta Univ. Uppsala, Uppsala, Sweden, 1979.

Engelund, F., and J. Fredsoe, Sediment ripples and dunes, *Ann. Rev. Fluid Mech.*, *14*, 13–37, 1982.

Flemming, B. W., The role of grain size, water depth and flow velocity as scaling factors controlling the size of subaqueous dunes, in *Marine Sandwave Dynamics Workshop*, edited by A. Trentesaux and T. Garlan, pp. 55–60, Serv. Hydrogr. et Oceanogr. de la Mar., Lille, France, 2000.

Fluit, C. C. J. M., and S. J. M. H. Hulscher, Morphological response to a North Sea bed depression induced by gas mining, *J. Geophys. Res.*, *107*, 3022, 10.1029/2001JC000851, 2002.

Hervouet, J. M., and P. Bates, The TELEMAC Modelling System (Special issue), *Hydrol. Proc.*, *14*, 2000.

Hervouet, J. M., and L. Van Haren, Telemac 2D Version 3.0-Note de principe, *Tech. Rep. HE-42/94/052/A*, 91 pp., EDF-SOGREAH, Grenoble, France, 1994.

Hibma, A., H. J. de Vriend, and M. J. F. Stive, Channel and shoal formation in estuaries, paper presented at 2nd IAHR Symposium on River, Coastal and Estuarine Morphodynamics, Int. Assoc. of Hydraul. Eng. and Res., Obihiro, Japan, 2001.

Houbolt, J. J. H. C., Recent sediments in the southern bight of the North Sea, *Geol. Mijnbouw*, *47*, 245–273, 1968.

Hulscher, S. J. M. H., Tidal-induced large-scale regular bed form patterns in a three-dimensional shallow-water model, *J. Geophys. Res.*, *101*, 20,727–20,744, 1996.

Hulscher, S. J. M. H., and G. M. van den Brink, Comparison between predicted and observed sandwaves and sand banks in the North Sea, *J. Geophys. Res.*, *106*, 9327–9338, 2001.

Huthnance, J. M., On one mechanism forming linear sand banks, *Estuarine Coastal Shelf Sci.*, *14*, 79–99, 1982.

Jelgersma, S., Sea-level changes in the North Sea basin, in *The Quaternary History of the North Sea*, edited by E. Oele, R. T. E. Schuttenhelm, and A. J. Wiggers, pp. 233–248, Acta Univ. Uppsala, Uppsala, Sweden, 1979.

Knaapen, M. A. F., S. J. M. H. Hulscher, and O. Scholl, Can we predict the growth of sandwaves? Hindcast of a field experiment in the Bisanseto Sea, Japan, in *Proceedings of Coastal Engineering 2000*, vol. 3, pp. 2661–2671, Am. Soc. Civ. Eng., Reston, Va., 2001.

Komarova, N., and A. Newell, Nonlinear dynamics of sand banks and sandwaves, *J. Fluid Mech.*, *415*, 285–321, 2000.

Langhorne, D. N., A study of the dynamics of marine sandwave, *Sedimentology*, *29*, 95–110, 1982.

Le Bot, S., D. Idier, T. Garlan, A. Trentesaux, and D. Astruc, Dune dynamics: From field to measurements to numerical modeling: Application to bathymetric survey frequency in the Calais-Dover Strait, in *Proceedings of the Marine Sandwave Dynamics Workshop*, edited by A. Trentesaux and T. Garlan, pp. 101–108, Serv. Hydrogr. et Oceanogr. de la Mar., Lille, France, March 2000.

Moshagen, H., B. Thorbjornsen, P. Strass, B. Latteux, and M. Venturi, The Norfra Pipeline: Challenging shore approach handled by coastal dynamics modeling, paper presented at Seventh (1997) International Offshore and Polar Engineering Conference, Int. Soc. of Offshore and Polar Eng., Honolulu, Hawaii, May 25–30, 1997.

Peltier, E., and B. Latteux, TSEF Version 3.1-Note de principe, *Tech. Rep. HE-42/95/062/A*, 21 pp., EDF-SOGREAH, Grenoble, France, 1995.

Peltier, E., J. Duplex, B. Latteux, and P. Pechon, Finite element model for bed-load transport and morphological evolution, in *International Conference on Computer Modelling in Ocean Engineering*, vol. 2, edited by A. S. Arcilla et al., A. A. Balkema, Brookfield, Vt., 1991.

Spaink, G., Analyse Noordzeeboring N, gelegen op de West Hinder Bank (in deutch), *Internal Rapp. 136-afd*, Macropaleont., Geol. Dienst, Harrlem, Holland, 1963.

Stride, A. H., *Offshore Tidal Sands-Processes and Deposites*, 222 pp., Chapman and Hall, New York, 1982.

van der Molen, J., and H. E. de Swart, Holocene tidal conditions and tide-induced sand transport in the southern North Sea, *J. Geophys. Res.*, *106*, 9339–9362, 2001.

Van Rijn, L. C., Handbook of sediment transport by currents and waves, *Rep. H 461*, 1002 pp., Delft Hydraulics, Delft, Netherlands, 1989.

Veenstra, H. J., Gravels of the Southern North Sea, *Mar. Geol.*, *7*, 449–464, 1969.

D. Astruc, Institut de Mécanique des Fluides de Toulouse, Allée Pr. Camille Soula, 31400 Toulouse, France. (astruc@imft.fr)

D. Idier, Faculty of Engineering, Water Engineering and Management, University of Twente, P.O. Box 217, 7500 AE Enschede, Netherlands. (D.Idier@ctw.utwente.nl)